Steering mirror design and dynamic controls for a dual-actuation platform using high-strain actuators

Shane C. Woody*
InsituTec Inc., Charlotte, NC, 28213
and
Stuart T. Smith†
University of North Carolina at Charlotte, NC, 28223

This manuscript discusses several novel design approaches to enhance dynamic precision of electro-mechanical positioning systems. In particular, a detailed development program for fast steering mirrors is addressed and various unique metrology and motion control strategies are presented. In general, material developments are continually advancing lightweight mirror structures such as the implementation of silicon carbide (SIC) materials to provide higher mechanical bandwidth response. Additionally, electro-mechanical actuators must continue to advance in conjunction with the mirror technologies in order meet stringent performance specifications (i.e. power requirements, weight, and precision dynamic response). The technologies developed through this development effort include; ultra-high strain piezoelectric actuators for enhanced motion control performance, a novel mechanism design employing a dual actuation platform to provide high bandwidth response and long-range, high-precision capability, innovative controller methodologies for the series coarse/fine system and active attenuation of dynamic reaction forces, integration of energy absorbing foams to enhance dynamic control, and real-time precision digital controllers.

I. Introduction

This manuscript addresses the development of a large lightweight 300 mm diameter fast steering mechanism. The objective is to extend these efforts to a high bandwidth steering mirror for defense and satellite communication. Fine steering mirrors are generally flat mirrors located aft of the secondary optics of a typical optical train[1, 2]. Mechanical beam steering mirrors are typically used to enable accurate pointing and, because of platform vibration and jitter, they must be able to mitigate high frequency components up to several kHz[3]. The goal of this 6 month program was to design, fabricate, and integrate a state of the art 9 degree of freedom steering mechanism, see Figure 1 for overview of subcomponents. The project involved several state of the art technologies in the following areas;

- Dual actuation mechanism to enhance closed loop control
- Nonrotationally symmetric honeycomb structure to enhance structural stiffness
- Ultra high strain single crystal actuators with advanced actuation characteristics
- Energy absorbing foam to attenuate high frequency instabilities
- High bandwidth precision high voltage amplifiers
- Active force attenuation to mitigate reaction forces to the optical work bench

II. Dual Platform Methodology (coarse and fine actuation platforms)

The aim of the fast steering mechanism (FSM) is to combine the closed loop capability of a long range platform while maintaining high bandwidth response of a short range actuator[4, 5, 6]. This design approach uses two piezoelectrically actuated motion-control platforms integrated in series[7], Figure 2 to Figure 4. The complete mechanical device shown in Figure 2 represents a three-tier system with the following sections;

* Senior Engineer, InsituTec Inc., 9625-B Vinca Circle, NC 28213

† Professor, Mechanical Engineering, University of North Carolina at Charlotte, Center for Precision Metrology, 9201 University City Blvd, CARC 151,,Charlotte, NC 28223

- Top high bandwidth (HBW) Platform: mirror actuation platform with real-time dynamic response
- CentralPlatform: long range (LR) motion control platform
- Lower Platform (RF): lower platform attenuates reaction forces generated by LR and HBW platforms

First, the LR platform is mounted on top of three long PMN-PT stacked actuators. This is shown further in Figure 3 where the mirror has been removed. The LR platform rigidly connects three short, high bandwidth, stacked actuators to provide short range closed loop control to the mirror platform. As shown in Fig. 2, the HBW platform is connected to the top of the LR platform. The two actuators or platforms in conjunction serve to provide long range motion control while simultaneously providing dynamic positioning control. Essentially, the fine platform provides high resolution and high speed to eliminate the high bandwidth following errors of the coarse platform. In this design, two distinct advantages arise, inherently lower inertia (which may be designed into the target platform) and low signal to noise.

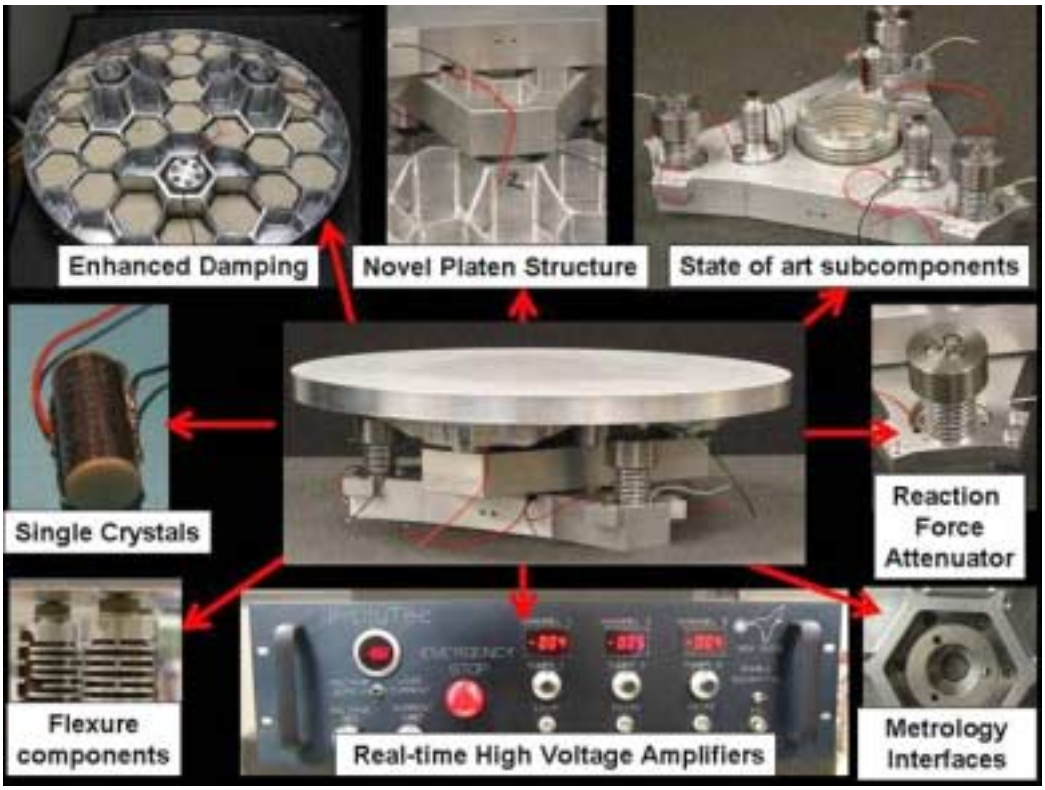

Figure 1. Overview of steering mechanism components.

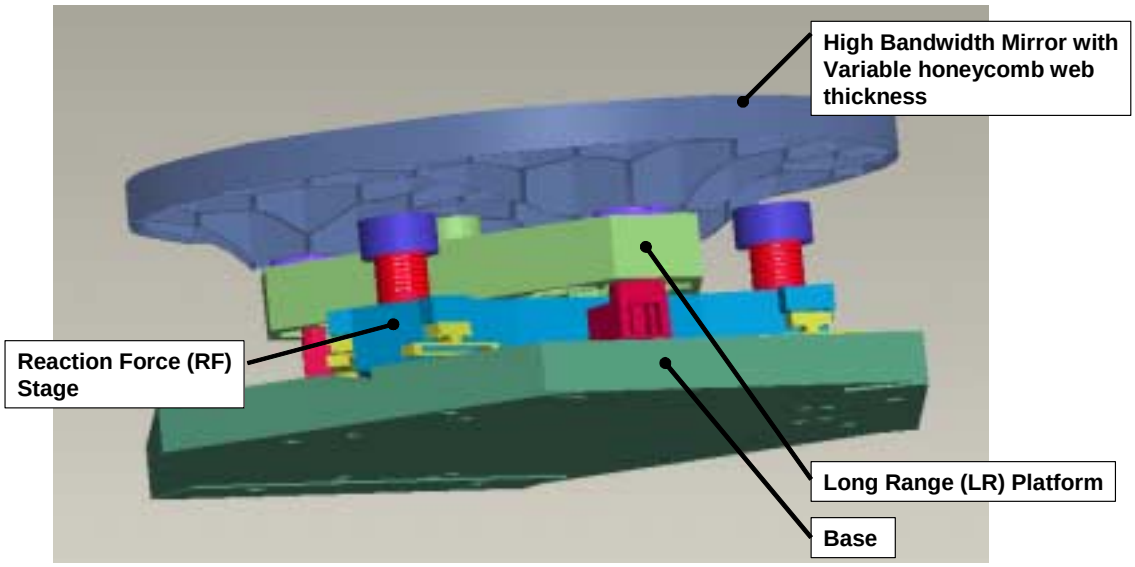

Figure 2. Side view showing completed FSM design.

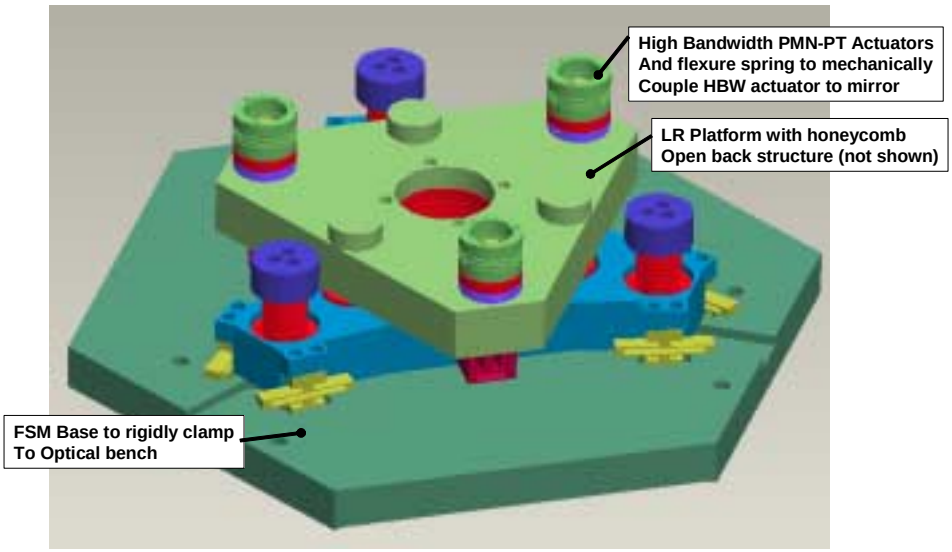

Figure 3. Top view of FSM design with platen removed.

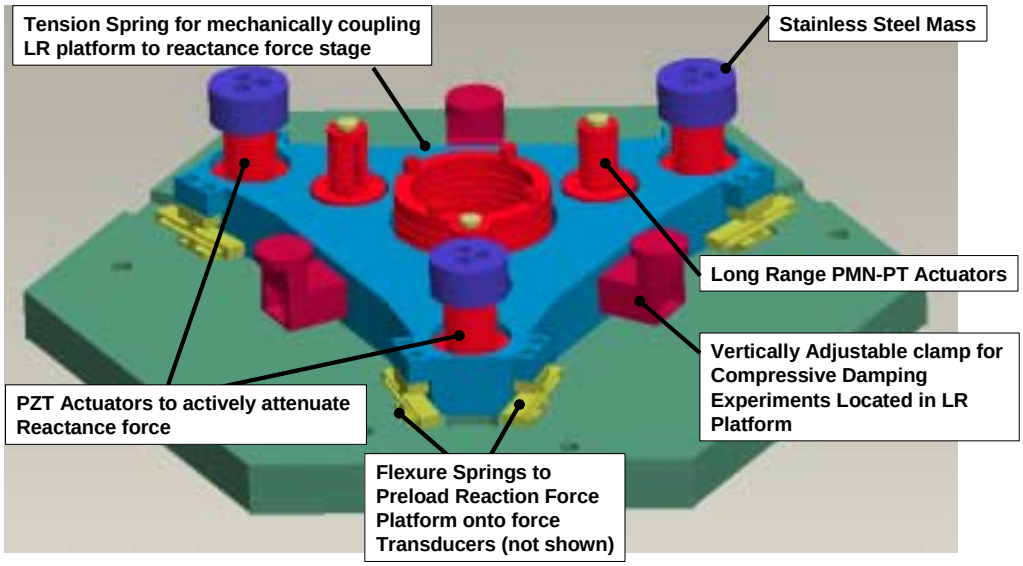

Figure 4. Top view of FSM design with platen and LR platforms removed.

III. Non-rotationally Symmetric 300 mm Platen Design

A bending moment occurs on the mirror at the actuator positions from the drive force generated by the actuators. This force is a combination of the forces necessary to accelerate the moving components of the assembly as well as the distortions of the preload springs and rotating contacts of the coupling between actuator and mirror. Thus, the mirror needs to be designed with the highest mechanical stiffness located closest to the actuator position in order to minimize distortions. Building upon previous efforts in the field of high bandwidth steering mirrors, a new design is presented with a non-rotationally symmetric open back structure, Figure 5. As shown, the back of the platen is designed with webs which vary in height. The objective is to provide higher stiffness at the actuator platen interface and taper the platen's stiffness down further away from the interface region.

Several design configurations for the large lightweight 300 mm mirror were analyzed using finite element models, Figure 6. These investigations use a low cost substitute material (aluminum) for the mirror platen instead of a SiC to validate the models for the dual platform design. Each structure was modeled using an aluminum and various geometries were assessed (note that frequencies will scale directly as the square root of the specific stiffness of the material of the mirror for a given geometry). Table 1 gives the parameters and first mode frequency for a variety of possible designs. For example, model 6A is a conventional uniform, honeycomb, open-back structure. The additional models evaluated the methodology of varying height structures. As shown, a maximum of 28% improvement was determined between model 6A and 5D. This demonstrates that the structure with variable web height is poised to provide higher dynamic performance compared to conventional uniform honeycomb structures.

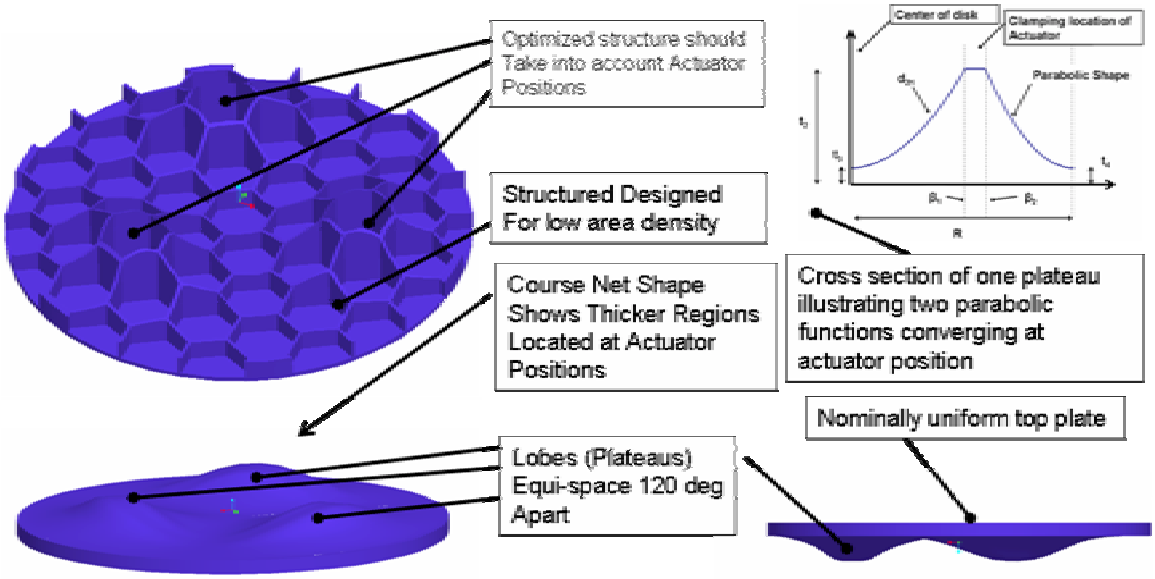

Figure 5. Overview of non-rotationally symmetric open back structure.

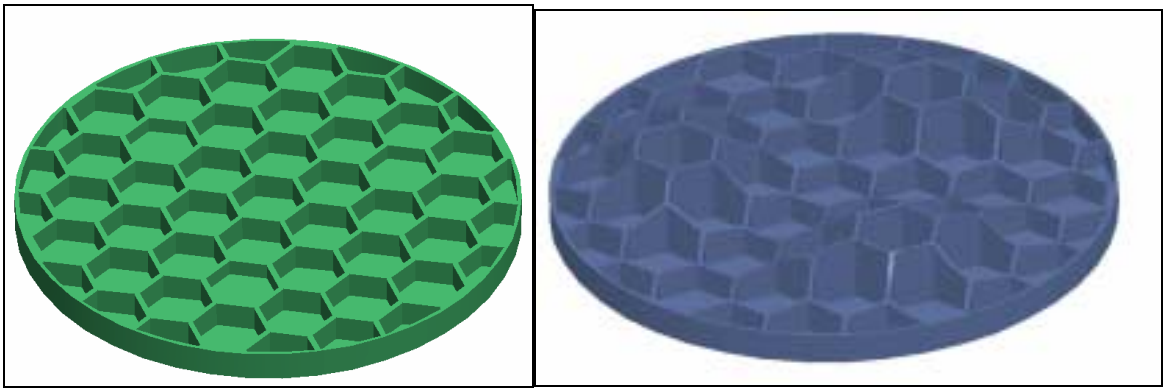

a) **b)**

Figure 6. Mirror comparison (a) conventional open-back honeycomb structure (b) non-rotationally symmetric open back honeycomb structure.

Table 1. Description of assessed models.

Model Name	Uniform Variable Thickness	Web Thickness (mm)	Floor Thickness (mm)	Weight (g)	First Mode (Hz)
Model 6A	No	3.0	2	950	1057
Model 5C	Yes	3.0	3.0	940	1352
Model 5D	Yes	2.0	2.0	950	1487
Model 5F	Yes	2.0	1.5	850	1521
Model 5G	Yes	2.0	1.0	773	1546

A complete 300 mm diameter platen was manufactured based upon the non-rotationally symmetric design described above, Figure 7. The platen is designed with a first mode above 1.2 kHz and a target weight of approximately 850 grams. The FSM platen has been high speed machined on a Makino A55, Figure 7. The aluminum platen is fashioned from a workpiece mounted in a picture frame style work holding. After the platen's honeycomb structure and surface contour are machined, the outer rim of the platen is machined to the floor with a

thickness of 0.15 mm. This thin floor provides the operator with the capability to easily cut the platen from the 'picture frame'. The total machining time was approximately 2.5 hours and furthermore could be optimized less than 2 hours if required. The rapid completion of the platen is contributed to proven tool tuning and chatter theory techniques which significantly optimize the cutting speeds for the machining center[8, 9]. Furthermore, these same techniques may be readily applied to alternative materials such as SIC materials.

Figure 7. Manufactured platen representing the 300 mm mirror (manufactured in 2.5 hours).

IV. Ultra High Strain Single Crystals

In general, piezoelectric stacked actuators are routinely found throughout precision applications (such as fast steering mechanisms) requiring real-time motion control. However, typical piezoelectric actuator compositions are capable of producing maximum strains of around 0.1-0.15%. Consequently, long stacked actuators are often necessary to produce sufficient displacement. As the actuator is increased in size, the mechanical system's footprint and mass increase resulting in lower mechanical bandwidths and higher power requirements. Single crystals based on (1-x)Pb(Mg1/3Nb2/3)O3-xPbTiO3 (PMN-PT) represents a piezoelectric material that can achieve 4 to 10 times the strain of conventional ceramic piezoelectrics with comparable deliverable actuation force[10, 11, 12, 13, 14, 15]. The attributes of single crystals relevant to adaptive structures include:

- Piezoelectric coefficients (d_{33}) in excess of 2000 pm V^{-1} and field induced strains > 0.5% (a factor of 5 increase over piezoelectric and electrostrictive ceramics).
- Blocking forces equivalent to conventional piezoelectric and electrostrictive ceramic.
- Very low strain electric field hysteresis for high strain precision (equivalent to electrostrictive PMN-PT ceramic).
- Very high transverse piezoelectric coefficients (d_{32} better than -1200 pm V^{-1}).
- Very high shear piezoelectric coefficients (d_{15} better than 2500 pm V^{-1}).
- Crystal actuators can be constructed at the same size (and operating voltage) as piezoelectric or electrostrictive ceramic actuators but with 5 times the displacement.
- Crystal actuators can be made with the same displacement as conventional devices but have up to a 5 times shorter length (and therefore 5 times lower weight) or up to 5 times lower operating voltage.
- Cryogenic performance is comparable to conventional piezoelectric displacements operating at room temperature.
- Low hysteresis resulting in less heat dissipation
- Two times greater strain energy density compared to ceramic-based devices.

During this project, several different types of ultra-high strain PMN-32%PT stacked actuators were produced by TRS Technologies and delivered to InsituTec for assembly and testing. These stacks were 10 mm in diameter and each active layer is 0.5 mm thick. Several different active layers were tested which included 3, 5 and 40 active layers. Initial tests by TRS Technologies demonstrate the high strain potential in the 40 active layers, Figure 8(a). As shown in the left graph, the strain reaches 0.35% at 20 kV cm^{-1}. Theoretically, single plate elements have achieved significantly higher electric fields > 100 kV cm^{-1} which is a factor of 5 higher than currently measured. However, the stacked actuators have only been assessed below 20-30 kV cm^{-1}. Part of this limitation is due to high voltage arcing across the plates and would need to be further investigated and the stacks may need to be redesigned to accommodate high voltages. Nonetheless, the PMN-32%PT generates 3 times higher strain at 20 kV cm^{-1} compared

to leading piezoelectric actuators. Furthermore, the active plate elements could be manufactured thinner and thereby provide high strains at the same voltage levels.

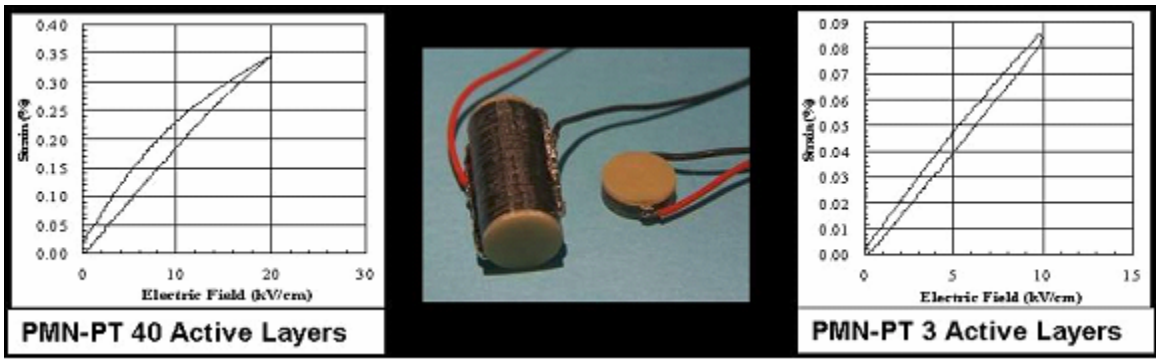

a) **b)** **c)**

Figure 8. Comparison between 40 active layer and 3 active layer PMN-PT stack actuators (a) strain vs. applied electric field for the 40 active layer stack (b) photograph of the 40 and 3 active layer stacks (c) strain vs. applied electric field for the 3 active layer stack.

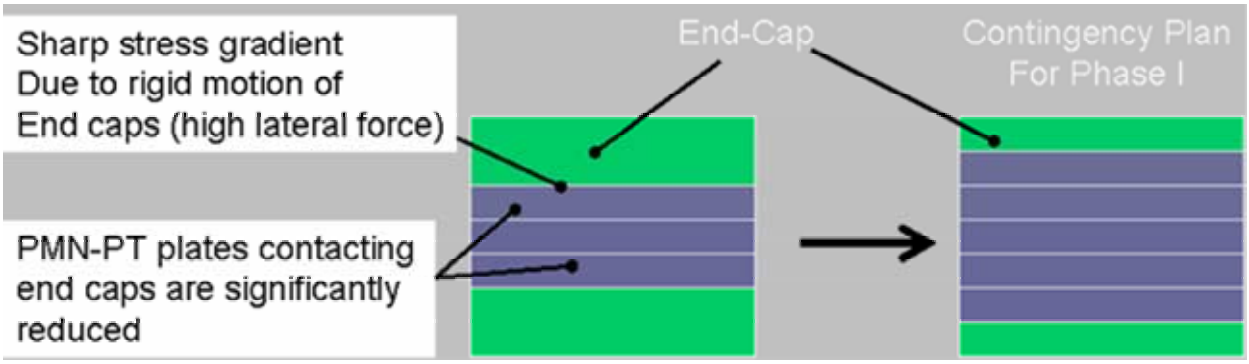

Figure 9. Two stack configurations for the short stack PMN-PT.

The second set of PMN-PT stacks is significantly shorter and is employed for the high bandwidth platen. The short stack originally was designed with 3 active layers. The results are shown in Figure 8(c) on the right side of the figure. In this case, the stack provided significantly less strain compared to the 40 active layer stack. The strain for the stack with 3 active layers has half of the strain (for the same electric field) compared to the stack with 40 active layers. This is results from the sharp stress gradient located at the endcap and PMN-PT interface, illustrated in Fig. 9. As shown, the PMN-PT expands in the d_{33} direction and additionally contracts in the lateral direction (due to Poisson's effect). The lateral force at this interface causes the adjacent PMN-PT to be constrained and therefore lowers the maximum allowable strain. Several techniques may be applied to increase the displacement output. During this project, the stacks were redesigned with 5 active layers. The additional two active layers provide further displacement and slightly better strain overall. Alternatively, the shorter stacks could be redesigned with thinner plate elements. The thinner plate elements (i.e. < 0.2 mm instead of 0.5 mm) would provide higher strain output for the same applied voltage. A further investigation would involve variably thick plate elements instead of uniform plate elements. Essentially, the end-cap and PMN-PT interface generates a very large stress gradient which may generate failure over time. In this case, plate elements would gradually increase in thickness from the center of the stack to the outside of the stack. The outside plate elements would provide lower strain compared to the inside plate elements and thereby provides a gradual stress gradient across the boundary layers. To provide preload forces, the stacked actuators are inserted into the manufactured flexure[16] mechanisms shown in Figure 10. This shows a variety of photographs of the flexure mechanisms.

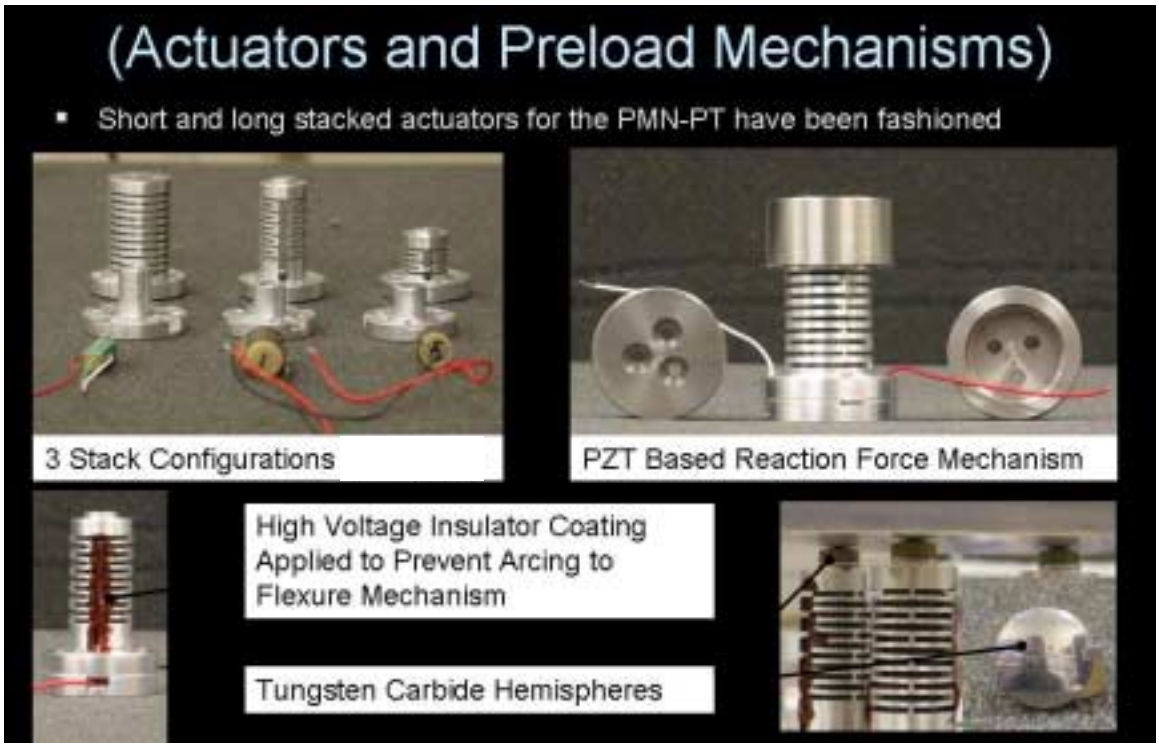

Figure 10. Photograph of the flexure mechanisms.

A test stand was devised employing a flexure mechanism with an inherent stiffness of 2.7 N μm^{-1}, Figure 11. The stiffness of this mechanism is a factor of 30 higher compared to the FSM mechanism. The higher stiffness will generate a fractional lost motion due to the inherent stiffness of the external mechanism. The first set of experiments compared the 3 and 5 active layers stacks, Figure 12. As shown, the 3 active layer produced approximately 2 µm at 1000 V (i.e. 20 kV cm^{-1}) and the 5 active layer stack produced approximately 6 µm at 1000 V. As a result of higher displacement, the 5 active layer stack was employed in the FSM top platform. Additionally, Figure 12 demonstrates the stacks generate low displacement with insufficient preload. Generally, the stacks are preloaded to 100-200 N in order to provide an adequate interface between the stack layers and thus minimize the effects of lost motion.

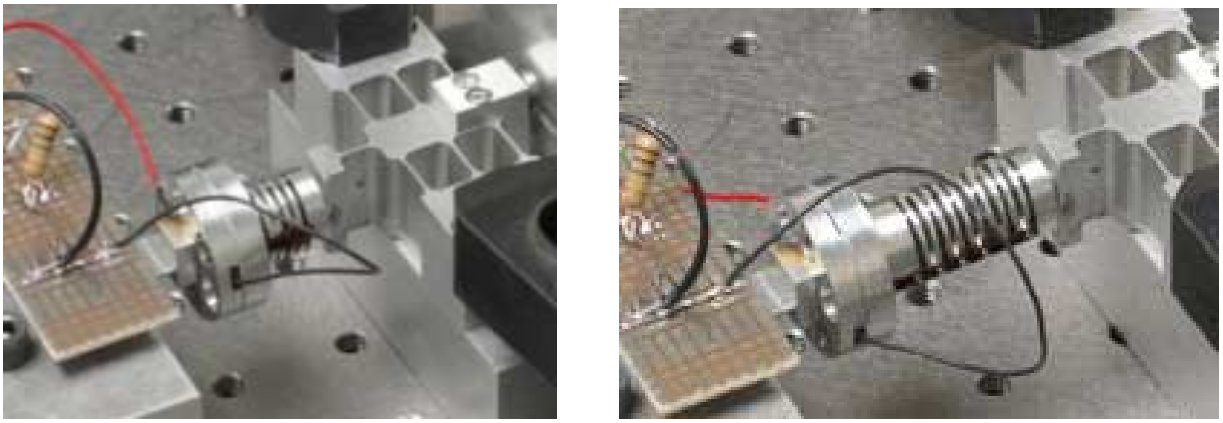

a) **b)**

Figure 11. Test stand to test the PMN-PT stacked actuators (a) short stacked actuator employing 5 active layers and preloaded in a flexure mechanism (b) long stacked actuator employing 40 active layers in a flexure mechanism and preloaded in a flexure mechanism.

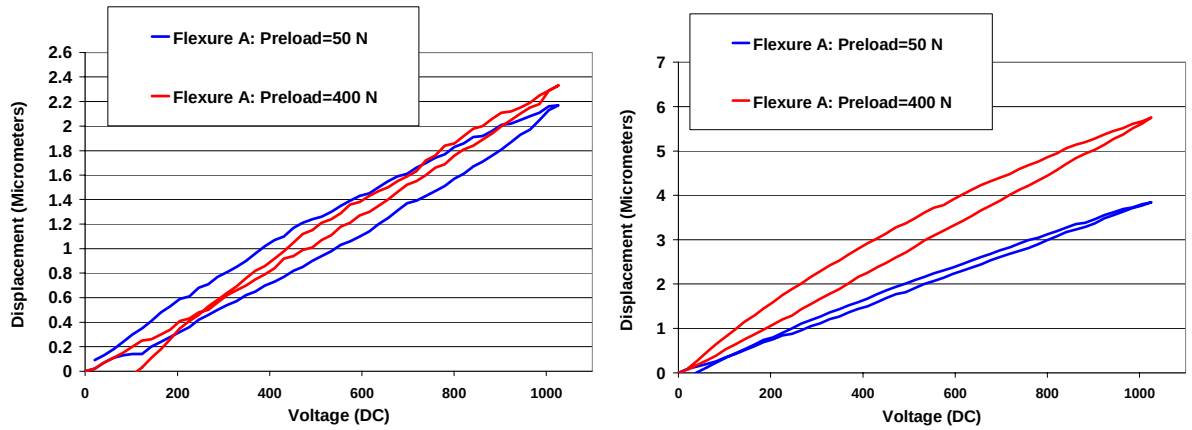

a) **b)**

Figure 12: Displacement vs. voltage (a) 3 active layer (b) 5 active layer

The 40 active layer stack was tested up to 1000 V and is shown in the test stand in Figure 11(b). The results obtained are shown in Figure 13. In Figure 13(a) the stacks are measured in a free condition with no mechanical impedance added to the stack. This technique produced a strain of 0.35% at 1000 V. In Figure 13(b) the same stack is measured in the test stand and the strain is measured. For this case, the maximum strain at 1000 V was 0.25%. This reduction in strain is directly due to the high stiffness of the mechanical flexure in the test stand. The stiffness of the FSM is significantly less than the test stand therefore it is expected that the strain would be improved in the FSM mechanism.

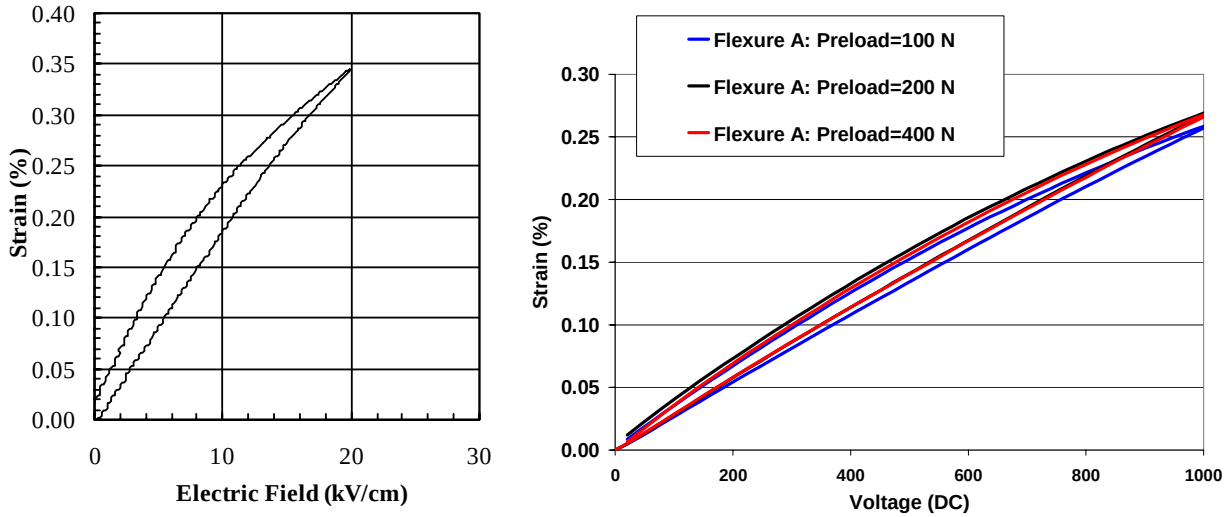

a) **b)**

Figure 13. Strain versus electric field and voltage for the 40 active layer stack (a) data measured in a free condition with no mechanical impedance added to the stack (b) data measured with the same stack coupled with a mechanical impedance of 2.7 N μm^{-1}.

Subsequently, the 40 active layer PMN-PT is compared with the PZT stacked actuators which are used in the reactance force attenuator (see section XII). Since the PZT stack has the same active layer length compared to the PMN-PT stack, the output strain may be directly compared. Each stacked actuator is inserted into the flexure mechanism and the stack was measured for strain vs. electric field, Figure 14. As shown, the PMN-PT generated twice the strain compared to the conventional PZT stack. Additionally, the PZT stack is limited to approximately 15 kV cm^{-1} and the PMN-PT is theoretically limited to >100 kV cm^{-1}. However, the PMN-PT stack actuators are recommended to remain at 20-30 kV cm^{-1} in order to prevent high voltage arcing.

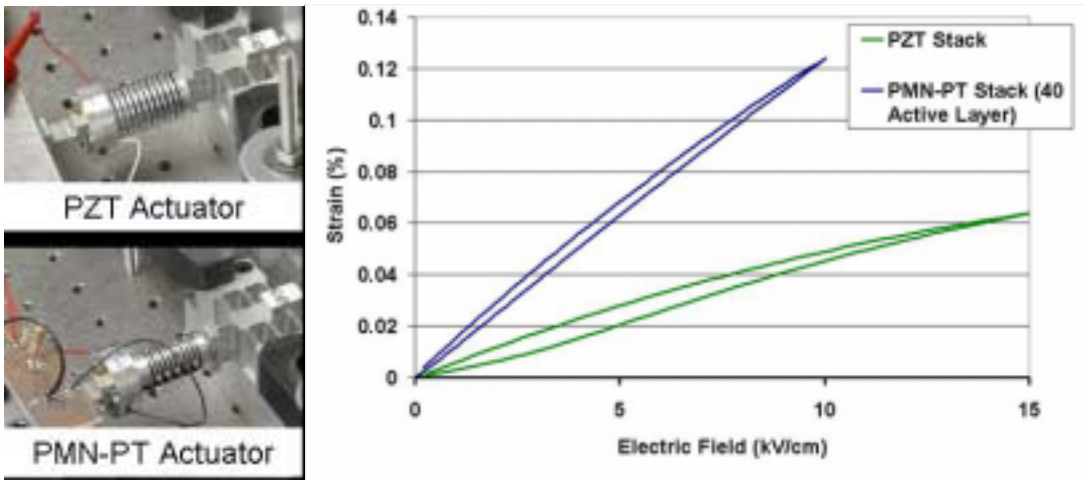

(a) **(b)**

Figure 14. Comparison between PZT & PMN-PT actuators (a) photographs of the PZT and PMN-PT actuators mounted into the test stand (b) strain vs. electric field.

V. Platen Acoustical Damping (Implementation of Energy Absorbing Foam)

In general, damping in a mechanism system should enhance the dynamic servo characteristics[17]. Two methods to provide higher closed loop control bandwidth are to

- Increase the natural frequency
- Increase damping to the system

These two methodologies are apparent in Eq. (1) which defines a limit to the closed loop control integrator gain K_I producing a 90 degree phase lag which adds to the 90 degree lag at the first mode resonance. In the absence of other factors effecting phase shifts in the system, this yields an upper limit for the controller gain governed by

$$\frac{2\pi f}{K_I} \geq G_I \tag{1}$$

where G_I represents the magnitude of the gain of the open loop system response at the natural frequency, K_I is the integrator gain and f is the natural frequency. Eq. (1) may be further represented in decibels, Eq. (2)

$$20\log\left(\frac{2\pi f}{K_I}\right) - 20\log(G_I) = 0 \tag{2}$$

Therefore, 3 dB attenuation would correspond to a 20% increase in the integrator gain term. Likewise, an increase in the integrator gain will provide a faster closed loop controlled response. As a result, the 300 mm diameter platen's open-back honeycomb structure (see Figure 7) is explored in conjunction with energy absorbing foams (purchased from EAR Corporation). The foams are strategically placed inside the honeycomb pockets[18]. Based upon recent literature from Varanas and Nayfeh[19, 20], energy absorbing foams are expected to attenuate high mode resonant frequencies without adding significant mass. These investigations have shown frequency mode attenuation above 600 Hz resulting by coupling the foam to a mechanical structure. The attenuation is suggested to result from the capability to generate a standing wave within the foam. In general the added damping will benefit the control dynamics by making them less susceptible to disturbances due to a lower 'Q' value. Therefore, the controller's tunable parameters (i.e. such as PID) may be further optimized and provide faster settling times.

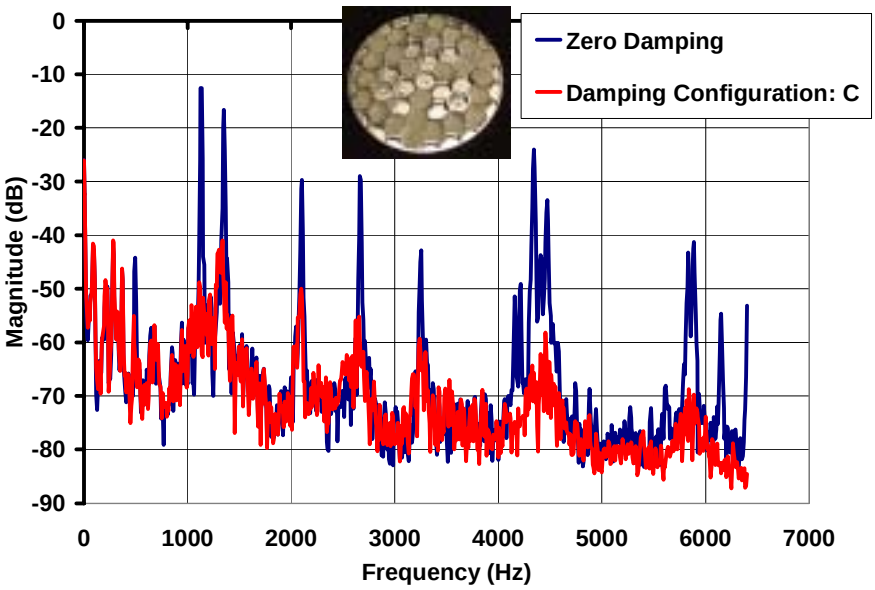

Figure 15. FRF for damping configuration C compared to zero damping.

The substrate was setup on an optical bench and a spectrum analysis was assessed using a spectrum analyzer. A small aluminum rod with a cross sectional area of 5.0 x 5.0 mm^2 was contacted underneath the platen at the central location. This is chosen in order to contact the platen at a node. The first set of experiments assessed the platen with free-free boundary condition. An impulse is applied to the platen with a plastic rod and the frequencies are monitored with an acoustical microphone. The microphone's signal is transferred to a spectrum analyzer. A FRF measurement is employed over 0-6.5 kHz. In this series of experiments, a total of 10 damping configurations were explored and the optimal configuration is shown in Figure 15. As shown, the energy absorbent foam attenuated the higher modal frequencies by 25-50 dB. This dramatic attenuation provides unique advantages for mechanical structures such as the honeycomb open-back structure. The critical design parameters for these types of structures are the natural frequency and the overall mass of the platen.

VI. High Bandwidth High Voltage Amplifiers

During the project effort, two three channel high voltage power amplifiers were developed to accommodate the high bandwidth and high voltage requirements for the single crystal actuators. The two units are constructed with three channel high voltage outputs varying from 0-1000 V and 0-300 mA. Furthermore, the two enclosures were constructed with different RC cut-off filters. Type I enclosure is constructed with a 10 kHz cut-off filter and type II is constructed with a 30.3 kHz cut-off filter.

Characterization of the open loop response for the two different high voltage amplifiers was undertaken. A piezoelectric cylinder with an 8 nF capacitive load served as the test load for each amplifier channel. A step response from a signal generator is transferred to the high voltage reference and the output is connected to the capacitive load. The output signal is transferred through a 100:1 voltage divider and monitored using a data acquisition system. As shown in Figure 16, the rise time and fall time are measured for type I and II amplifiers. The type I provides a rise time of 280 µs and a rise time of 480 µs. The type II is further enhanced and provides a rise time of 90 µs and a fall time of 180 µs. Due to the enhanced dynamic performance, the type II amplifiers will be employed for the high bandwidth platform and the type I amplifiers will be employed for the long range platform.

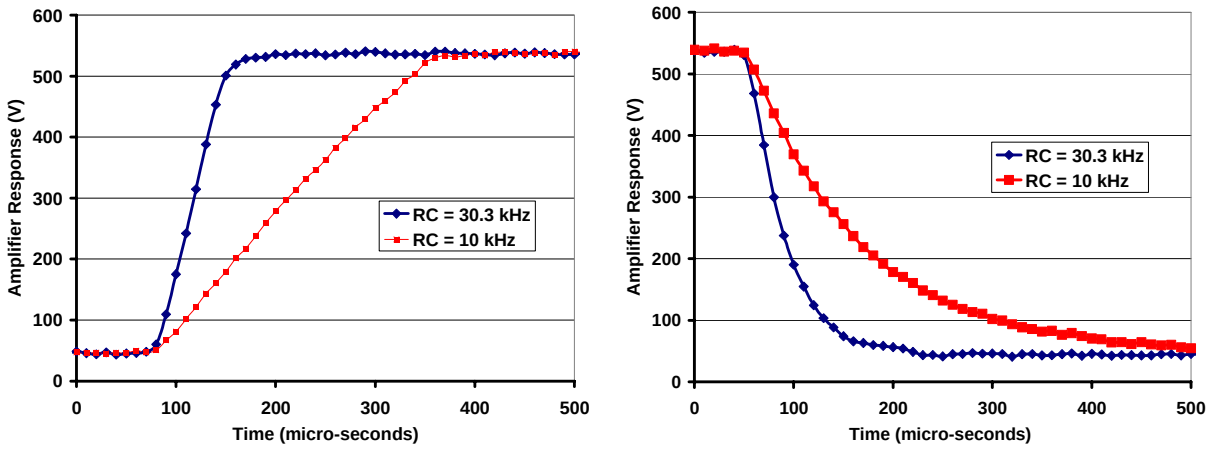

Figure 16. Settling time for the two amplifier versions (a) rise time of the RC cutoff filter of 30.3 kHz provides a rise time of 90 µs and the RC cutoff filter of 10 kHz provides a rise time of 280 µs (b) Fall time for the two amplifier versions, an RC cutoff filter of 30.3 kHz provides a fall time of 180 µs and the RC cutoff filter of 10 kHz provides a rise time of 450 µs.

Additionally, the open loop response is measured for the gain and phase margin, Figure 17. As shown, the gain margin crosses over -3 dB at 1496 Hz for the type I amplifier and greater than 5000 Hz for the type II amplifier. The phase margin is approximately 48º at 1496 Hz and the type II amplifier provides significantly less phase lag compared to the type I amplifier. The open loop response will be enhanced with feedforward controllers assuming the trajectory or commanded future signal is known.

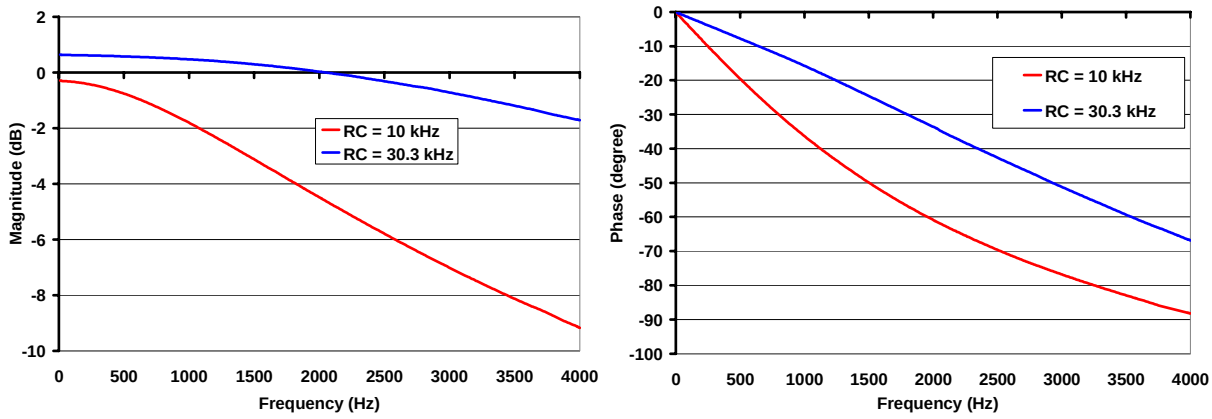

Figure 17. Open loop response for the type I and II amplifiers (a) gain margin (b) phase margin.

VII. Closed Loop Control Experimental Stand

The next step involved the experimental characterization of the FSM mechanism. The FSM mechanism and metrology fixture are shown in Figure 18. The metrology fixture comprises four capacitive-based displacement sensors with a signal bandwidth of approximately 10 kHz and a resolution of approximately 50 nm. Four sensors are rigidly attached to the metrology fixture by way of squeeze clamp fixture and these subsequently monitor the motion of the top platform relative to the fixed frame. The sensors are positioned 100 mm from the center of the platen (that emulates the dynamic mirror load) and equispaced 90º apart.

Figure 18: Fast steering mechanism and metrology fixture

VIII. Controller Algorithms

A dSPACE™ digital controller with 100 ksps sampling rate, 16 bit precision and multichannel ADC and DAC capability is employed for the experimental program. The dSPACE™ digital controller and Matlab's Simulink™ were used to provide a simple and effective method to implement the controls. First, a transformation matrix is derived to convert the four capacitive sensors and transfer these signals to the coordinates θ_x, θ_y, and Z axis. This transformation matrix is based upon the following Eq. (3) – Eq. (5).

$$\theta_X = \frac{(P_2 - P_1)C_1}{L} \tag{3}$$

$$\theta_Y = \frac{(P_3 - P_4)C_2}{L} \tag{4}$$

$$Z = \frac{(P_1 + P_2)C_1 + (P_3 + P_4)C_2}{4} \tag{5}$$

The distance, L, is 200 mm and the calibration coefficients for each set of two sensors are C_1 is 0.0127 µm V^{-1} and C_2 is 0.0254 mm V^{-1}. The three equations above would need to be further multiplied by 10^6 to convert to µRad. The transformation matrix to convert the four signals to these respective coordinates is shown as Eq. (6).

$$\begin{bmatrix} -63.5 & 63.5 & 0 & 0 \\ 0 & 0 & 127 & -127 \\ 3.175 & 3.175 & 6.35 & 6.35 \\ 0 & 0 & 0 & 0 \end{bmatrix} \begin{bmatrix} P_1 \\ P_2 \\ P_3 \\ P_4 \end{bmatrix} = \begin{bmatrix} \theta_X \\ \theta_Y \\ Z \\ 0 \end{bmatrix} \tag{6}$$

Next, the transformation matrix is determined for the coarse and fine platforms to convert the two rotations and single translation drive signals to the appropriate single crystal actuators.

$$\theta_X = \frac{A_2 - A_3}{L_2} \tag{7}$$

$$\theta_Y = \frac{A_1 - \left(\frac{A_2 + A_3}{2}\right)}{L_1} \tag{8}$$

$$Z = \frac{A_1 + A_2 + A_3}{3} \tag{9}$$

The corresponding distances between the actuators rotating about θ_x is L_2 = 95.956 mm and the distance L_1 is 83.1 mm. Therefore, the transformation is derived as Eq. (10).

$$\begin{bmatrix} \theta_X \\ \theta_Y \\ Z \end{bmatrix} = \begin{bmatrix} 0 & \frac{1}{L_2} & -\frac{1}{L_2} \\ \frac{1}{L_1} & -\frac{1}{2L_1} & -\frac{1}{2L_1} \\ \frac{1}{3} & \frac{1}{3} & \frac{1}{3} \end{bmatrix} \begin{bmatrix} A_1 \\ A_2 \\ A_3 \end{bmatrix} \tag{10}$$

However, the inverted transformation matrix needs be multiplied by the coordinate matrix in order to transfer the appropriate signals to the actuator matrix. Therefore, the coordinate transformation matrix from Eq. (10) is inverted and multiplied by the coordinate matrix, Eq. (11).

$$\begin{bmatrix} \theta_X \\ \theta_Y \\ Z \end{bmatrix} \begin{bmatrix} 0 & 55.4 & 1 \\ 44.5341 & -25.7106 & 0.9282 \\ -44.5341 & -27.6996 & 1.0718 \end{bmatrix} = \begin{bmatrix} A_1 \\ A_2 \\ A_3 \end{bmatrix} \tag{11}$$

Similarly, the top platform's transformation matrix is given by

$$\begin{bmatrix} \theta_X \\ \theta_Y \\ Z \end{bmatrix} = \begin{bmatrix} -\frac{1}{L_3} & 0 & \frac{1}{L_3} \\ \frac{1}{2L_4} & -\frac{1}{L_4} & \frac{1}{2L_4} \\ \frac{1}{3} & \frac{1}{3} & \frac{1}{3} \end{bmatrix} \begin{bmatrix} B_1 \\ B_2 \\ B_3 \end{bmatrix} \tag{12}$$

The transformation matrix is inverted and multiplied by the coordinate matrix to yield

$$\begin{bmatrix} \theta_X \\ \theta_Y \\ Z \end{bmatrix} \begin{bmatrix} -71.9665 & 41.55 & 1 \\ 0 & -83.1 & 1 \\ 71.9665 & 41.55 & 1 \end{bmatrix} = \begin{bmatrix} B_1 \\ B_2 \\ B_3 \end{bmatrix} \tag{13}$$

Once the transformation matrices are derived the control algorithms can be written to control the platform. Prior to initial testing with the mechanism, a voltage bias of 80 volts is initially transferred to the coarse and fine platform actuators. This is required to provide a sinusoid commanded response about a fixed mean value from 100-500 Hz. The frequency response from the platform's sensors is measured and the magnitude and phase are plotted over this frequency range.

Based upon the FRF response, it was possible to determine the coupling between each degree of freedom, Figure 19. These figures show the frequency response coupling between degrees of freedom for the coarse platform. For example, Figure 19 drives the platform about θ_x and detects the motion in θ_x, θ_y and Z directions. The θ_x drive and θ_x detection demonstrates a high system gain at 100 Hz with approximately 75 dB. However, θ_y and Z motions are approximately 38 and 25 dB respectively. In terms of the angular coupling this is a 36 dB reduction corresponding to response in one axis to a drive in the other being reduced by a factor of 63 or 1.6 % cross-coupling. The top high bandwidth platform produced similar results and therefore is not shown in the report.

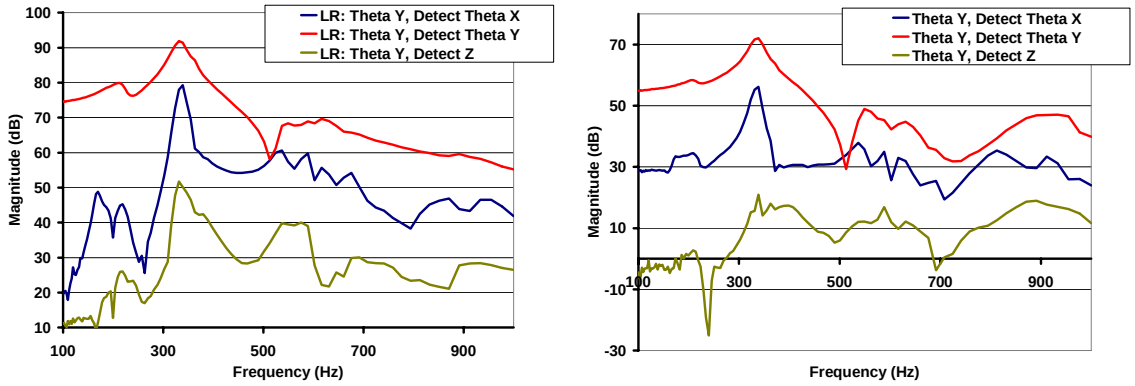

a) **b)**

Figure 19. FRF of θ_y to assess coupling between degrees of freedom (a) LR (coarse platform) (b) HBW (high bandwidth) platform.

IX. Mechanism modes

During this experiment, the dynamic modes of the top platform were assessed. In this case, the top platform is completely disassembled in order to decouple the frequency modes found in the lower platform. The mechanism's frequency response function is measured for θ_x, θ_y and Z directions, Figure 20 demonstrates θ_x. The rotational response of the system clearly shows the low natural frequency to occur at 416 Hz and a zero occurring at 512 Hz. This is a similar response as measured in the complete mechanism. The rigid body dynamics for the top platform was calculated to be greater than 3 kHz but the platen's first mode response is measured at 1100 Hz. Furthermore, Z axis frequency response measured a first mode at 1100 Hz which would correspond to the platen's mode. The rotational response provides a significantly lower dynamic response then initially predicted. The cause of the low dynamic mode is assumed to be the contact interfaces of the flexure, bolts, or stacked actuators. A second redesign effort would investigate the mechanical interface to eliminate this rotational mode.

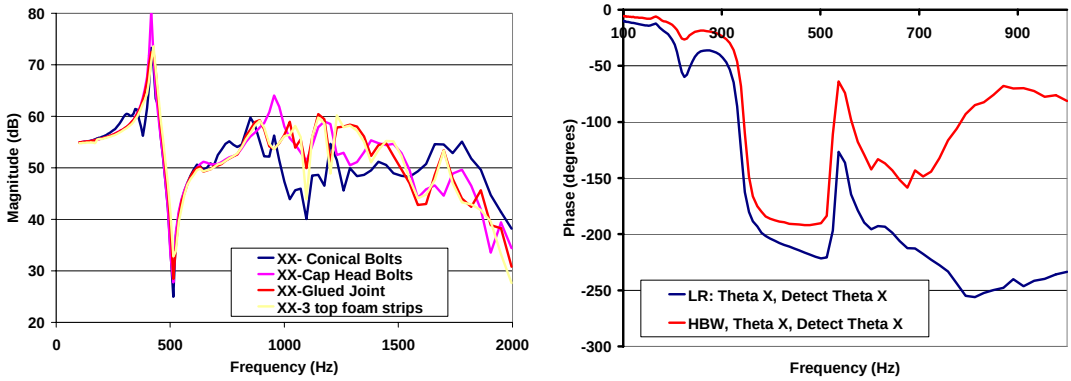

a) **b)**

Figure 20. FRF of top platform in θ_x direction (a) magnitude (b) phase.

X. Feedforward vs. Conventional Control

A control algorithm was developed for the single and dual platforms. This control algorithm may be used to control the stages independently or simultaneously for each degree of freedom. The first set of tests assessed the *Z* direction for closed loop control. The short range platform was initially tested with a sinusoidal input at ±1.0 µm amplitude at 300 Hz, Figure 21. A simple integrator was first applied and the gain term is optimized. As shown in this figure, the following error produces a ±0.9 µm error with only an integrator controller. The next controller algorithm implemented two types of feedforward algorithms which included acceleration, velocity, and feedforward algorithms. In general, feedforward algorithms significantly enhance the overall performance of the platform. However, this can only be implemented if the trajectory is predicted or known several samples ahead and will be investigated in future work. The following error for a 300 Hz closed loop control motion was reduced to less than 0.07 µm. This provides a factor of 9 improvement compared to a simple integrator controller. Similarly, the top platform was controlled with a ramp function as the input. The ramp function's following error was reduced to less than 0.1 µm by employing the feedforward control algorithm.

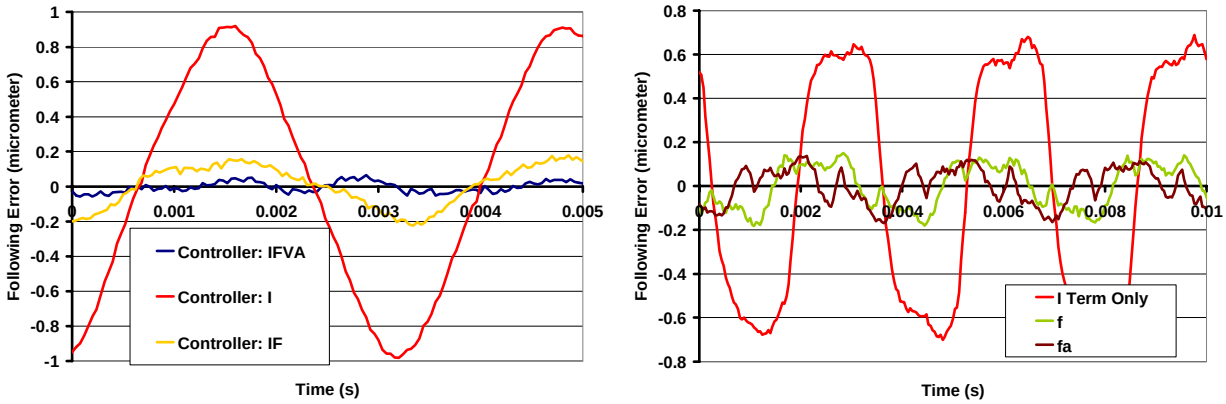

Figure 21. Following error in the short range platform when controlling the platen in the *Z* axis at 300 Hz at an amplitude of ± 1 µm (a) with a sinusoidal input (b) with a ramp input.

The next set of tests assessed closed loop control for rotation. Figure 22 represents the actual response of the both the long range and short range platforms (independent of each other) while rotating about the *X* axis. This is referred to as θ_x. First a control signal command is provided with a sinusoidal input at 300 Hz and an amplitude of ±20 µRad for the short range platform. The following error in Figure 22(a) demonstrates the conventional and feedforward algorithms. In general, a 6% following error was produced at 300 Hz using the feedforward techniques.

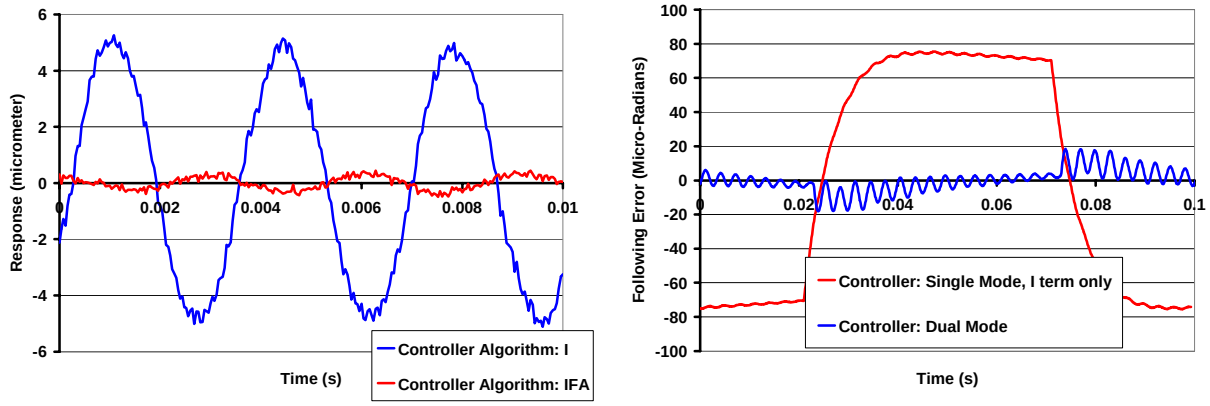

a) **b)**

Figure 22. (a) Following error of the short range platform in closed loop controlled for θ_x at 300 Hz and ± 20 µRad (b) Following error of the long range platform with an integrator and feedforward controller in closed loop control for θ_x at 10 Hz and ± 300 µRad

The maximum range for the coarse platform below 500 volts is measured at ±300 µRad. As shown, a ramp function is employed at 10 Hz for the coarse platform and an integrator and feedforward algorithms are assessed, Figure 22(b). Finally the closed loop controlled response of the long range platform for θ_x at 1 Hz and ±500 µRad was measured with an applied voltage between 0-1000V. The maximum rotational angle was measured at approximately ±500 µRad.

XI. Dual Platform vs. Coarse Platform

Investigators used the control algorithm to control both the coarse and fine platforms during coarse positioning. This methodology is chosen to enhance the controller dynamics of the coarse stage. First, a sinusoidal response operating at 10 Hz and ± 10 µm was employed to control the *Z* axis motion. The coarse platform was controlled first and the control parameters were optimized. As shown in Figure 23(a), the following error for the coarse platform was optimized to ± 0.7 µm. Next, the fine and coarse platforms were simultaneously implemented and the following error was reduced to ± 0.1 µm. The dual platform enhances the following performance by a factor of 7. The next step assessed a ramp function demand for the *Z* axis direction. Similarly, the following error for the ramp function is significantly improved with the dual axis system compared to only controlling the coarse platform, Figure 23(b).

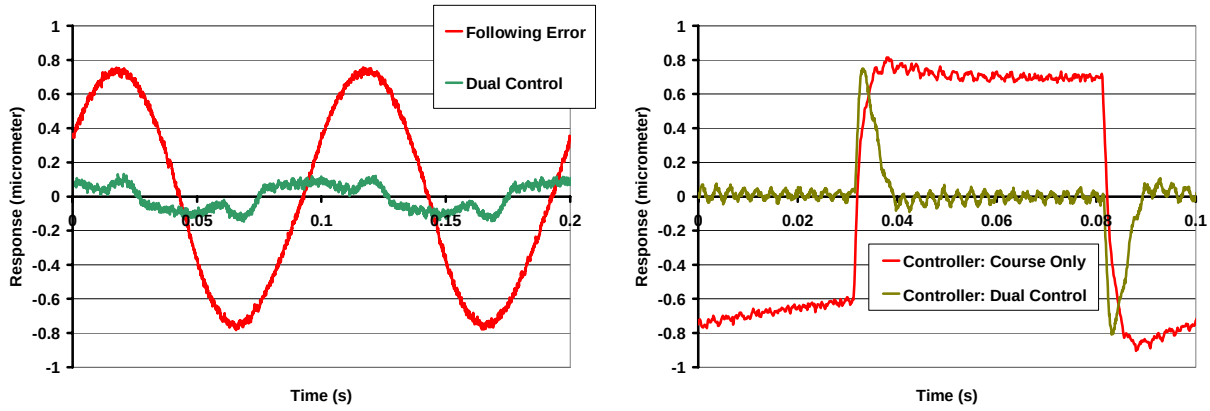

a) **b)**

Figure 23. Closed loop controlled response for *Z* for 10 Hz and ±10 µm following error employing coarse and dual control (a) for a sinusoidal input (b) for a ramp input.

The final experiment investigated closed loop control for one of the rotational axis, θ_x. A sinusoidal command operating at 10 Hz and ±300 µRad was implemented, Figure 24(a). The coarse platform was tuned with an optimized integrator gain and the following error was measured at 111 µRad. Next, the dual platforms controller was implemented and the following error was measured at ± 5 µRad. As shown, the following error was improved by a factor of 20 compared to a conventional integrator controller.

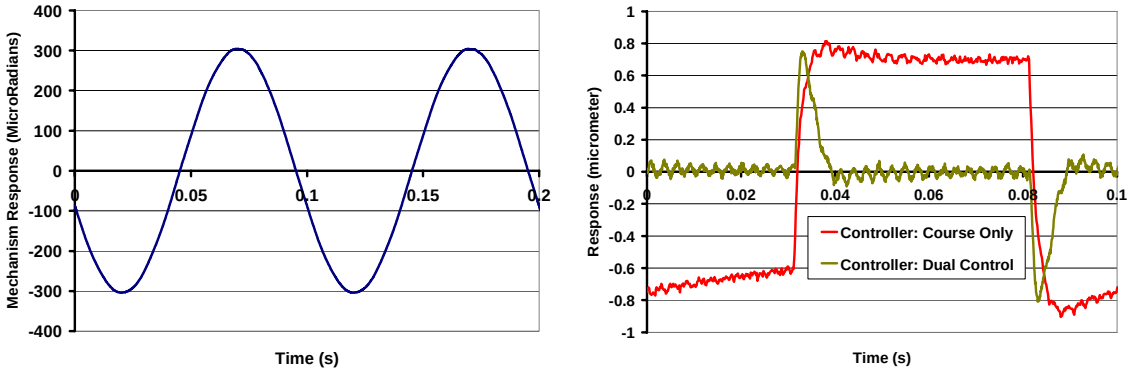

a) **b)**

Figure 24. Closed loop controlled response for θ_x for ±300 mRad at 10 Hz (a) platform response (b) following error employing coarse and dual control.

XII. Reaction Force Attenuator

In general, reaction forces propagating to the optical work bench should be attenuated by 80-100%. One methodology is to provide a rotating counter balance to attenuate the reaction force. However, this methodology suggests considerable weight added to the overall structure as well as increased complexity to the overall design. Alternatively, an active control of actuators driving relatively simple masses to generate an equal and opposite reaction force to the platform may be designed. An example of this approach is represented in Figure 25. In this case, the fine and coarse platforms remain the same and are mounted to a Reaction Force (RF) platform as shown. The RF platform is then mounted to a fixed base, which is then bolted to an optical test bench (in practice, to reduce mass, this fixed base may be eliminated). Additionally, the RF platform's mounting points (structural loop) are coupled through a PZT sensor. This type of sensor is employed to monitor the reaction forces transmitted to the fixed based. Next, piezoelectric stacks with added mass are mounted underneath the RF platform (in our final design these have been inverted). As shown from Figure 25, the mass of the combined HBW and LR platforms will generate an inertial force due to acceleration. Therefore, the inertial force may be eliminated with a counteracting inertial force generated by the acceleration of mass M_R as shown.

Under ideal conditions, the inertial forces at each end of the platform will cancel identically giving the following relation;

$$F = \frac{I\ddot{\theta}}{2L} = M_R 4\pi^2 f^2 \frac{X}{2} \tag{14}$$

where $\ddot{\theta}$ is the maximum angular acceleration generated by the platform, X is the reaction force actuator stroke, f is the closed loop drive frequency. Therefore, the drive frequency may be easily determined

$$f^2 = \frac{I\ddot{\theta}}{LM_R 4\pi^2 X} \tag{15}$$

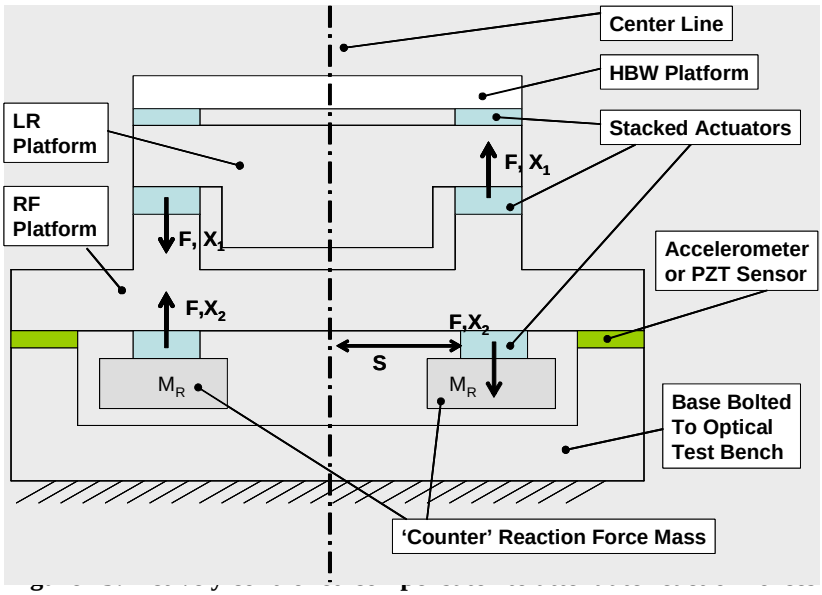

Based on the above equations, an active compensator was developed, Figure 26. Based on the above equations, an active compensator was developed. In this photograph, a stainless steel cylinder is mounted on top of a PZT actuator. The mass, M_r, is 60 grams, the actuators are spaced 99.0 mm from the center and the actuator has a total stroke of 10 µm. Additionally, the RF platform is placed on top of three force transducers and further preloaded to the lower base.

An open loop sinusoidal frequency at 100 Hz is generated in the coarse platform and the force transducers are measured. As shown in Figure 27, the force transducer signal generates ±1 volt output. Next, the PZT actuator with stainless steel block is turned on with the same frequency. The amplitude is adjusted until the reaction force is attenuated by 80%. This preliminary data represents a valid approach to actively attenuating reaction forces in real time.

a) b) c)

Figure 26. Reaction force attenuator (a) attenuator located in 3 locations on outside parameter of platform (b) attenuator configuration with stainless steel cylinder attached to PZT actuator (c) assembled mechanism with attenuator shown on outer periphery.

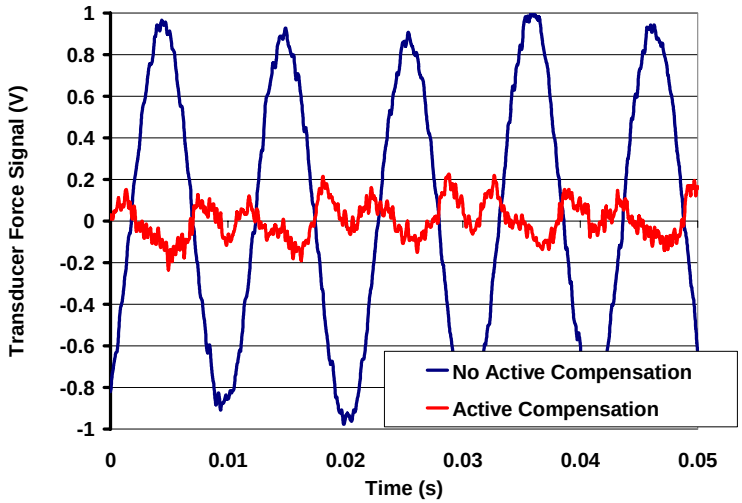

Figure 27. Transducer force signal while FSM mechanism is in open loop at approximately 100 Hz (A force signal is observed to attenuate by 80% when the active compensator is turned on).

XIII. Conclusions

Over a period of 6 months, several enabling technologies were amassed for the fast steering project. All of these technologies such as the dual platform methodology, energy absorbing foams, non-rotationally symmetric platen, single crystal actuators have successfully demonstrated enhanced performances for large lightweight steering structures. The single crystal actuators have demonstrated 0.35-0.4% strain rates which correspond to a factor of 4 improvement compared to conventional piezoelectric actuators. In general, the single crystal actuators will provide the necessary bandwidth and power requirements. However, a considerable number of further developments will be necessary to demonstrate a reliable functioning unit that can be integrated into various operating conditions. Future work will aim to develop a state of the art silicon carbide (SiC) turning mirror. Several SiC designs will be evaluated and the results obtained in this project (energy absorbent foams and non-rotationally symmetric platens) will be applied to the SiC structure. Also, the dual actuation platform (i.e. fine and coarse actuation platforms) have demonstrated remarkable results to enhance the dynamic performance of the coarse platform. These results clearly demonstrate a factor of 7-20 improvement in following error is achievable while simultaneously operating the coarse and fine platforms. Moreover, nonlinear controller algorithms have demonstrated significant improvement in closed loop control of the FSM. These algorithms were found to provide a factor of 9 improvement compared to conventional PID algorithms. Lastly, the reaction force attenuator demonstrated up to 80% attenuation while operating the coarse platform.

XIV. Acknowledgments

Authors are grateful to the Missile Defense Agency (MDA) for providing funding under contract HQ0006-04-C-7063 and Dr. Arup Maji at the AFRL/Space Vehicles Directorate for his technical support throughout this project. Furthermore, many of these investigations were carried out at UNC Charlotte's Center for Precision Metrology and authors would like to thank Bethany Woody for her technical support in machining the aluminum platen. Finally, the authors would also like to thank Paul Rehrig and Xiaoning Jiang at TRS Technologies for their technical support for which authors are very grateful.

[1]Germann L.M., "Specification of fine-steering mirrors for line-of-sight stabilization systems", *Proceedings of SPIE*, Vol. 1543, 1992, pp. 202-212.

[2]Glaese R., Anderson E., Janzen P., "Active suppression of acoustically induced jitter for the airborne laser", *Proceedings of SPIE*, Vol. 4034, 2000, pp. 151-164.

[3]Kral, Lukas, and Prochazka, "Satellite Laser Ranging Precision Ultimate Limit", *Proceedings of SPIE.* , Vol. 5240, 2004, pp. 26-30.

[4]Mori K, Munemoto T, Otsuki H, Yamagjuchi Y, Akagi K., "A dual-stage magnetic disk drive actuator using a piezoelectric device for a high track density", *IEEE Transactions on Magnetics*, Vol. 27, No. 6, 1991, pp. 5298-5300.

[5]Yao W., and Tomizuka M., "Robust controller design for a dual-stage positioning system", Proceedings of the IECON-International Conference on industrial electronics, control and instrumentation, Vol. 1, 1993, pp. 62-66.

[6]Schulthess, M.R., and Baugh S., "Digital control of the high-altitude balloon experiment auto-alignment system", *Proceedings of SPIE - The International Society for Optical Engineering*, Vol. 2468, 1995, pp. 206-218.

[7]Woody S.C., and Smith S.T., "Design and performance of a dual drive system for tip-tilt angular control of a 300 mm diameter mirror", submitted to Mechatronics, 2005, Not Published.

[8]Smith, S., Tlusty, J., "Current trends in high speed machining", ASME Journal of Manufacturing Science and Engineering, Vol. 119, 1997, pp. 664 - 666.

[9]Delio, T., Tlusty, J., and Smith, S., "Use of Audio Signals for Chatter Detection and Control," *ASME J. Eng. Ind.*, Vol. 114, 1992, pp. 146-157.

[10]Park S. and Shrout T., "Ultrahigh strain and piezoelectric behavior in relaxor based ferroelectric single crystals", *J. Appl. Phys.*, Vol. 82, No. 4, 1997, pp. 1804-1811.

[11]Hackenberger W., Rehrig P., Pan, M., and Shrout T., "Single crystal piezoelectrics for advanced transducer and smart structures applications", *Proceedings of SPIE*, Vol. 4333, 2001, pp. 92-103.

[12]Park S., Hackenberger W, "High performance single crystal piezoelectrics: applications and issues", *Current Opinion in Solid State and Materials Science*, Vol. 6, 2002, pp. 11–18.

[13] Park S. and Shrout T., "Characteristics of Relaxor-based piezoelectric single crystals for ultrasonic transducers", *IEEE Transactions on Ultrasonics, ferroelectrics and frequency control*, Vol. 44, No. 5, 1997, pp. 1140-1147.

[14]Woody S.C., and Smith S.T., "Performance comparison and modeling of PZN, PMN and PZT stacked actuators in a levered flexure mechanism", *Rev. Sci. Instrum.*, Vol. 75, No. 4, 2004, pp. 842-848.

[15]Woody S.C., Smith S.T., Jiang X., Rehrig P., "Performance of single crystal PMN-32%PT stacked actuators with application to adaptive structures", *submitted to Rev. Sci. Instrum.*, 2005, Not Published.

[16]Smith S.T., 2002, *Flexures: Elements of elastic mechanism design*, Gordon and Breach Science Publishers, Singapore, 2000

[17] Marsh E.R. and Slocum A.H., "An integrated approach to structural damping", *Precision Engineering*, Vol. 18, 1996, pp. 103-109.

[18]Woody S.C., and Smith S.T., "Damping of a thin-walled honeycomb structure using energy absorbing foam", submitted to Journal of Vibration and Controls, 2005, Not published.

[19]Varanas K.K., and Nayfeh S.A., "Damping of flexural vibration by low-density foams and granular materials", *Proceedings of DETC'03, ASME Design Engineering Technical Conference*, Vol. 5, 2003, pp. 1897-1905.

[20]Varanasi K.K., and Nayfeh S.A., "Damping of Flexural Vibration in the plane of lamination of elastic-viscoelastic sandwich beams", *Journal of sound and vibration*, Vol. 276, No. 3, 2004, pp. 689-711.